Tungsten-based bcc-superalloys

Parkes, Neal; Dodds, Russel; Watson, Andy; Dye, David; Hardie, Chris; Humphry-Baker, Samuel A.; Knowles, Alexander J.

DOI:
10.1016/j.ijrmhm.2023.106209

International Journal of Refractory Metals and Hard Materials 113 (2023) 106209

Contents lists available at ScienceDirect

International Journal of Refractory Metals and Hard Materials

journal homepage: www.elsevier.com/locate/IJRMHM

Tungsten-based bcc-superalloys: Thermal stability and ageing behaviour

Neal Parkes [a], Russel Dodds [b], Andy Watson [a,c], David Dye [b], Chris Hardie [d], Samuel A. Humphry-Baker [b], Alexander J. Knowles [a,b,d,*]

[a] University of Birmingham, Birmingham, UK
[b] Imperial College, London, UK
[c] Hampton Thermodynamics Limited, Hampton, UK
[d] United Kingdom Atomic Energy Authority, Culham Science Centre, UK

ARTICLE INFO

Keywords:
Refractory metal
Tungsten
Bcc-superalloy
Phase equilibria
Microstructure

ABSTRACT

Tungsten is considered as a primary material for the divertor and first wall in many fusion reactor designs. There has been further interest in nano-structured multi-phase tungsten alloys and composites, such as oxide dispersion strengthened alloys, where interfaces may be harnessed as defect sinks to improve irradiation resilience, whilst also improving base mechanical strength, and potentially ductility. Here we further investigate the concept of tungsten-based 'bcc-superalloys' within the W-Ti-Fe ternary system, comprising W-TiFe, A2-B2, *β-β'* nano-structures. Alloys were produced by arc melting and the microstructure controlled via thermal heat treatments, by solutionising at 1250 °C, followed by 750 °C ageing.

The alloys were characterised using electron microscopy, including composition measurements, alongside hardness measurements. Building on our previous work, we have demonstrated that nano-scale B2 TiFe(W) forms within A2(W,Ti,Fe) in the W-Ti-Fe alloys, creating localised regions of the targeted A2-B2 (*β-β'*) precipitate reinforced structure. Further, here we evaluated ageing at 750 °C, where within the interdendritic domains decomposition consistent with B2TiFe(W) -> B2 + A2 and A2(Ti,Fe,W) -> A2 + A3 is proposed. An experimentally validated preliminary W-Ti-Fe ternary phase diagram has been produced, helping to understand the stable phases present and instructing onward optimisation of W-superalloys as a candidate material for fusion energy.

1. Introduction

Tungsten (W) has the second highest melting point (after carbon) of all elements, at 3422 °C, and the highest of any metal. This gives tungsten the potential to provide exceptional high temperature structural integrity. Fusion reactors with plasma temperatures of 150 million kelvin represent some of the harshest conditions materials can be exposed to, and the high melting temperature makes tungsten a primary selected material, with the temperature of the divertor plate anticipated to be >1500 °C. Further, tungsten exhibits very low creep rates, low tritium retention and low sputter yields giving it great potential for extended use in fusion reactors [1].

However, tungsten has its drawbacks. It exhibits at high ductile to brittle transition temperature (DBTT), which for plate material can be 200–400 °C [2]. Furthermore, following irradiation the DBTT temperature rises yet higher, even as high at 800 °C. Alloying with rhenium is a well documented method to dramatically improve the DBTT of tungsten, however, this benefit may be lost following irradiation, due to irradiation induced precipitation [3]. New microstructure strategies such as oxide dispersion strengthened alloys (ODS) have been applied to tungsten [4] that could improve toughness and irradiation tolerance whilst also increasing creep strength, by analogy to ODS steels [3]. However, consistent large-scale production of ODS alloys remains a substantial challenge [5]. There is a need to devise new alloying and microstructure strategies to increase the resilience of tungsten in the fusion first wall.

Alloys based on a disordered A2 (bcc) system, such as tungsten, could theoretically be strengthened by precipitating an intermetallic phase that adopts an ordered superlattice structure of A2, such as B2, $L2_1$ or $D0_3$, shown in Fig. 1. This is an analogous concept to that more commonly found in the hugely successful fcc nickel-based superalloys, in which ordered gamma prime (γ') precipitates form within a disordered gamma (γ) fcc matrix. A bcc equivalent could therefore be considered β-β' [6,7].

Our recent work has demonstrated the 'bcc-superalloy'

* Corresponding author at: University of Birmingham, Birmingham, UK.
E-mail address: A.J.Knowles@bham.ac.uk (A.J. Knowles).

https://doi.org/10.1016/j.ijrmhm.2023.106209
Received 26 October 2022; Received in revised form 24 March 2023; Accepted 25 March 2023
Available online 30 March 2023

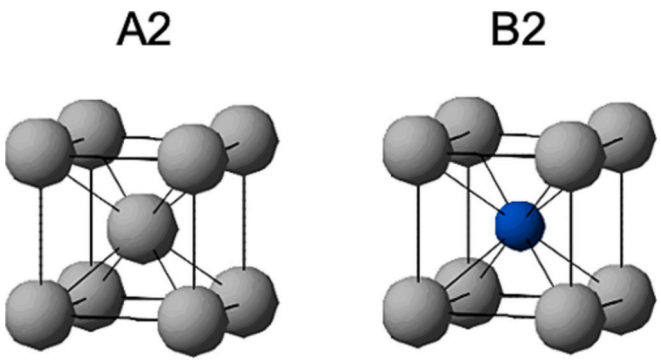

Fig. 1. Crystal structure of bcc A2 W, and superlattice ordered-bcc structure B2, e.g. TiFe, prototype CsCl.

microstructure concept is possible within beta titanium superalloys [8], and tungsten-based bcc-superalloys [9]. These use alloying additions of Ti and Fe to produce nanostructured tungsten, exploiting the phase equilibria in the W-Ti-Fe ternary phase diagram, see Fig. 5. These bcc-superalloys are intended to increase the strength of tungsten and irradiation damage tolerance, whilst further work is needed to understand the effect on DBTT and ductility. Careful selection of alloying additions can promote the formation of secondary reinforcing phases with a bcc matrix, namely the B2 intermetallic phase, forming a 'bcc-superalloy' microstructure of fine precipitates with semi-coherent interfaces, which can potentially act as internal sinks for irradiation damage, prolonging the operational life of the tungsten alloys in the fusion first wall. Interface sinks can allow the trapping of vacancies, enhancing the recombination with self-interstitial atoms, and trap He, suppressing bubble formation on grain boundaries. Furthermore, these second phases also strengthen and may improve the creep resistance of the alloys. The purpose of this work is to build on our first demonstration of a bcc tungsten superalloy in ref. [9] by investigating a different preparation route and the effect of secondary heat treatments to further optimise the microstructure.

2. Methods

W-Ti-Fe ternary alloys were made through vacuum arc melting at Imperial College London, from pure elements (99.9% purity) that were weighed out according to each alloy's target composition. These compositions were similar to those used in our previous work [9], but which were manufactured by ACI alloys inc. Due to one of the elements being tungsten, with a melting point of 3422 °C, it proved challenging to achieve a homogenous melt pool, with macro-segregation and some solid pieces of tungsten found in the casting. The ingots were inverted and remelted in order to improve compositional homogeneity, however significant macro-segregation remained.

The as-cast alloys were then sectioned appropriately for heat treatments. Each alloy was sectioned as to keep the individual pieces that were undergoing different heat treatments within the same vicinity of each other. This was to minimize the effects of macro-segregation from casting. This would mean that each sample of a given alloying composition would be much closer to each other, thus providing more comparable results between the as-cast and heat-treated conditions. Alloys underwent heat treatments followed by water quenching. After being encapsulated in evacuated argon backfilled quartz ampoules to prevent oxidation, the alloys underwent a 1250 °C for 100 h solution treatment in order to homogenise the two phases present and eliminate any micro-segregation, such as dendrite coring. Alloy WT60F was instead solution heat treated at 1100 °C for 100 h, to avoid melting. In contrast to our previous W-Ti-Fe work [9], here we then also applied a secondary ageing heat treatment, at 750 °C for 80 h, to promote further precipitation of the TiFe intermetallic phase. The furnaces used were controlled to an uncertainty of ±10 °C. Upon exiting the furnace after each treatment, the ampoules were water quenched, to avoid any unwanted phases forming on cooling.

Table 1
Tungsten-titanium-iron alloy with targeted compositions and measured compositions by at least six, 200 × 200 μm SEM EDX area scans from the as-cast condition on the JEOL 6400. Standard deviation shows variability from location to location due to macro-segregation.

	Target Composition			Measured Composition		
Alloy	W (at. %)	Ti (at. %)	Fe (at. %)	W (at.%)	Ti (at.%)	Fe (at.%)
WT60F	20	60	20	9.0 ± 1.0	69.9 ± 0.4	21.1 ± 0.7
WT40F	40	40	20	14.9 ± 5.4	59.6 ± 0.5	25.5 ± 4.9
WT30F	50	30	20	39.4 ± 4.0	39.8 ± 0.9	20.8 ± 1.4
WT20F	60	20	20	97.2 ± 0.3	2.6 ± 0.3	0.2 ± 0.1

Characterization was performed using scanning electron microscopy (SEM), carried out using a JEOL 6400, for initial imaging and energy dispersive x-ray (EDX) analysis, and Zeiss AURIGA and SIGMA 300 for higher resolution images of the nanoscale structures. The alloys were observed almost exclusively using the backscattered (BS) detector, and all SEM images contained within this article are in BS mode. This is because it provides atomic Z contrast imaging, and therefore was essential in helping to distinguish between the phases present. Furthermore, EDX area scans and point scans were used to determine average bulk alloy compositions and phase compositions, respectively.

Transmission Electron Microscopy (TEM) and scanning TEM (STEM) was also performed on a JEOL 2100+ TEM. Wire electrical discharge machining (EDM) was used to cut out 3 mm diameter cylinders from the alloys. From each cylinder three discs of approximately 0.25 mm thickness were cut and mechanically thinned and flattened, with their thickness brought to down to around 0.20 mm. The discs were then electropolished at −30 °C using perchloric acid and an electric potential, until electron transparent samples were created.

Vickers hardness values were collected, with 1 kg weight and a 10 s

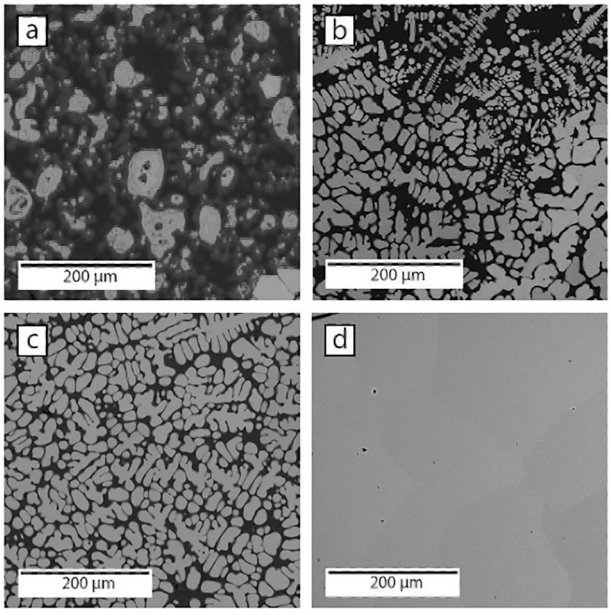

Fig. 2. SEM backscattered micrographs in the as-cast condition of (a) WT60F, (b) WT40F, (c) WT30F and (d) WT20F. Brightness is proportional to higher atomic Z.

dwell. At least six values were collected and averaged. Considerations were taken to account for any macro-segregation across the samples surfaces in order to provide the most accurate measurement possible. Indents were focused in regions with similar microstructures and compositions, which were representative of the alloy as a whole homogeneous sample, as observed and determined under the SEM.

3. Results and discussion

The tungsten-titanium-iron (W-Ti-Fe) system was selected for further investigation as a base system capable of producing a tungsten-based bcc-superalloys microstructure. The Fe content was kept constant for each alloy, whilst the W content was increased in place of Ti. The alloys are subsequently referred to as WTxF in which x is the target concentration of Ti, Fe held constant at 20%, with the balance being W, all in at.%.

3.1. As-cast

Firstly, the as-cast alloys were observed under SEM, with EDX the measured bulk area compositions shown in Table 1 (as well as the Target composition). SEM images of the four alloys in their as-cast state are shown in Fig. 2, (a) shows a large area of WT60F's surface where particles of solid tungsten can be seen with a Ti-rich matrix. For WT40F and WT30F, Fig. 2 (b) and (c) respectively, the formation of the bright W-rich dendrites are shown, with around 20–30 at.% Ti and very little dissolved Fe, around 2–3 at.% (Table 1). Additionally a Ti-rich inter-dendritic phase could be seen, containing approximately 60–70 at.% Ti with 20–40 at.% Fe, with ~2 at.% being W, which was found to have a low solubility in this phase. Moving on to WT20F in Fig. 2 (d) this region of alloy shows almost pure W, of composition >97 at.% W.

3.2. Solution heat treated

The alloys then underwent a solution treatment of 1250 °C for 100 h, except WT60F, which was heat treated at 1100 °C due to partial melting at 1250 °C. After the solution treatments all samples were water quenched. Fig. 3 shows the results of these treatments. The phase compositions of the four alloys measured by SEM-EDX are shown in Table 2. WT60F in Fig. 3(a) shows a reduction in pure W pieces previously seen in the as-cast microstructure (Fig. 2 (a)) and a higher volume fraction of the Ti-rich inter-dendritic phase. Additionally, W-rich dendrites were seen to exist and formed while some pure W pieces still remained, but these have shown signs of beginning to dissolve into the solution [8]. WT40F, WT30F and WT20F in Figs. 3 (b), (c) and (d) show the dendritic microstructure increasing in volume fraction with the increasing W content (bright features in Fig. 3, corresponding to W-rich compositions in Table 2). Point scans of the dendritic and inter-dendritic regions showed microsegregation due to coring has been largely eliminated, thus creating two more homogeneous phases in equilibrium with each other.

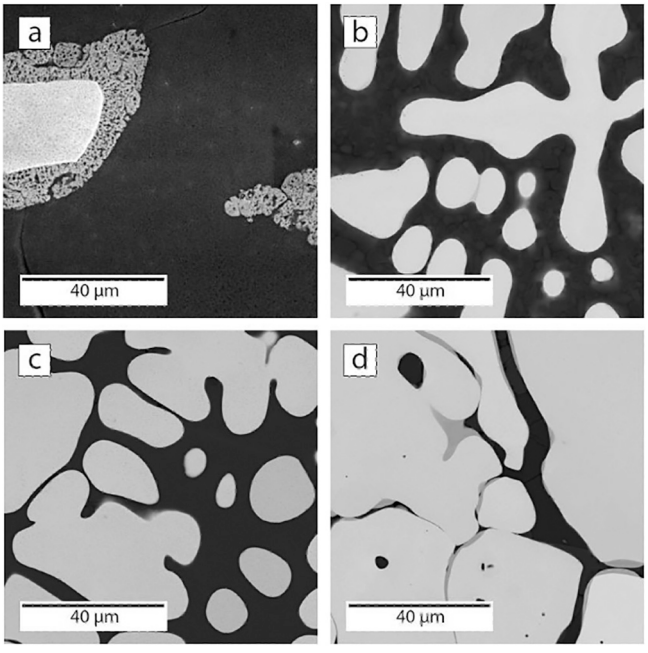

Fig. 3. SEM backscattered micrographs in the solution treated condition of (a) WT60F after 1100 °C for 100 h and (b) WT40F, (c) WT30F and (d) WT20F, all after 1250 °C for 100 h.

Table 2
Phases identified with individual phase compositions from each alloy in the solution treated condition. Measured using SEM-EDX point scans reporting average and standard deviation. (W-rich dendrites bright phase in Fig. 3).

Alloy	Phase	W (at.%)	Ti (at.%)	Fe (at.%)
WT60F	A2 Ti (inter-dendritic)	6.8 ± 0.5	69.2 ± 0.9	24.0 ± 1.3
	A2 W Dendrite	51.6 ± 0.3	41.1 ± 0.5	7.3 ± 0.6
	Pure W	98.9 ± 0.5	0.8 ± 0.6	0.3 ± 0.3
WT40F	A2 Ti (inter-dendritic)	2.4 ± 0.6	74.1 ± 3.3	23.5 ± 3.7
	A2 W Dendrite	71.4 ± 1.4	27.1 ± 1.5	1.5 ± 0.8
WT30F	A2 Ti (inter-dendritic)	2.3 ± 0.8	62.2 ± 0.4	35.5 ± 0.4
	W Dendrite	83.8 ± 2.9	13.9 ± 2.4	2.3 ± 0.7
	B2 TiFe (inter-dendritic)	2.7 ± 1.4	51.2 ± 0.7	46.1 ± 0.7
WT20F	A2 Ti (inter-dendritic)	2.0 ± 0.2	60.7 ± 0.7	37.3 ± 0.5
	A2 W Dendrite	81.2 ± 2.0	17.5 ± 1.6	1.3 ± 0.6
	A2 W Den. (2nd phase)	49.1 ± 1.2	44.5 ± 1.1	6.4 ± 0.9
	B2 TiFe (inter-dendritic)	3.0 ± 1.9	52.1 ± 1.5	44.9 ± 0.4

3.3. Solution heat treated and aged

Finally, all the alloys underwent the same ageing treatment at 750 °C for 80 h, and were water quenched, to drive the formation of nano-scale TiFe intermetallic within the tungsten rich phase. The results of which are shown in Fig. 4. WT60F in Fig. 4 (a) shows the development of an additional phase within the inter-dendritic region of the microstructure. These precipitates were too fine to be analysed by EDX point scans,

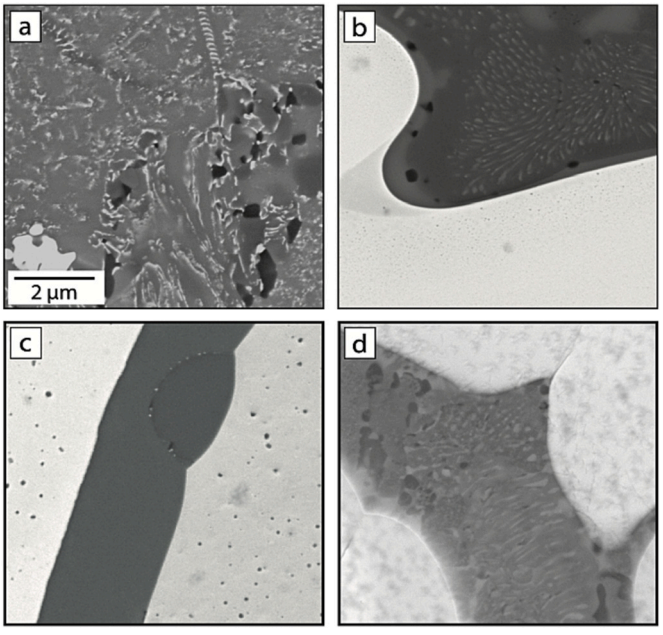

Fig. 4. SEM backscattered micrographs in the solution treated +750 °C aged condition of alloys: (a) WT60F, (b) WT40F, (c) WT30F and (d) WT20F.

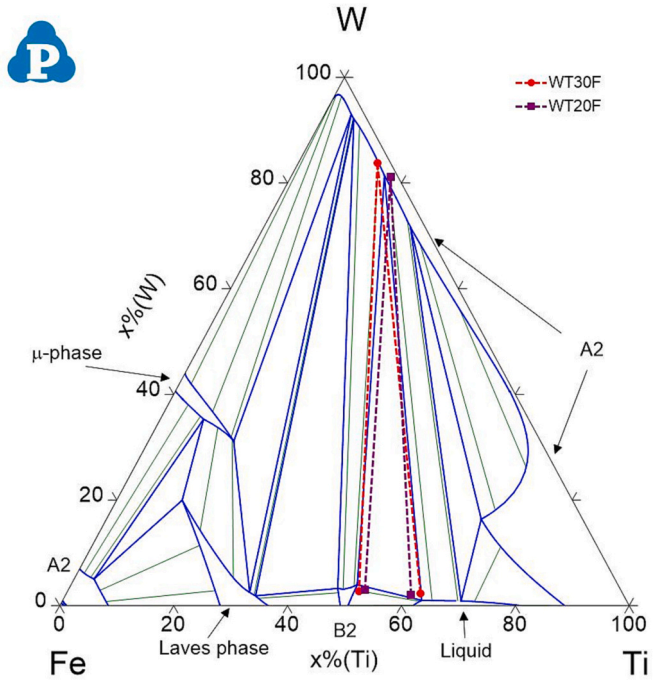

Fig. 5. Isothermal section of the W-Ti-Fe system for 1250 °C calculated using the thermodynamic description from [9], including SEM EDX data from Table 2.

however there is the possibility they could be identified using TEM (see Fig. 6). Inter-dendritic precipitates are seen in WT40F, and in WT20F to some degree (Fig. 4 (b) and (d)). Additionally, in WT30F, Fig. 4 (c), there are precipitates found to be forming within the W-rich prior dendrites. From knowledge of the ternary phase and by observing the compositional contrast, these are thought to be Ti and Fe-rich precipitates, and more namely the intermetallic TiFe [9] as observed in Ti-Fe-Mo alloys [11]. This would suggest B2 TiFe precipitates have formed within an A2 W-matrix, which was one of the goals set out of at the beginning of this project. The main three phases indicated by EDX were W-rich dendrites, the inter-dendritic Ti-rich phase and, in certain conditions, intermetallic TiFe. The W-rich dendrites were found to have W contents ranging from 71.4 to 83.8 at.%, Ti contents ranging from 13.9 to 27.1 at.% and very low Fe contents in the range of 1.3 to 3.5 at.%. The inter-dendritic regions were found to be Ti-rich and W-poor, with W contents from 1.0 to 2.4 at.% (disregarding WT60F because of its lower solution treat temperature), Ti contents of 51.0 to 74.1 at.% and Fe contents of 23.5 to 47.3 at.%. These large ranges of Ti and Fe content may suggest inaccuracies when measuring the correct phase, or may hint at different phases that decompose into other separate phases upon further heat treatments. Investigation with EDX point scans showed these areas have Ti contents of 49.1 to 52.2 at.% and Fe contents of 44.9 to 48.9 at.%, with minimal W contents of a few at.%. The formation of TiFe is not unexpected, as it is shown in the ternary phase diagram (Fig. 5), but it is one of the desired phases because of its B2 structure.

3.4. W-Ti-Fe ternary phase diagram

The new W-Ti-Fe composition data from SEM-EDX was compared to a preliminary assessment of the W-Ti-Fe system at 1250 °C after [9], shown in Fig. 5. The composition of the three-phases identified in Table 2 can be seen to be in agreement with the preliminary assessment [9]. A key aspect of this and our previous work [9] compared to the previous W-Ti-Fe ternary determination and assessment of Qiu & Jin [10], is the addition of tie lines to the W-rich A2(W,Ti,Fe) phase, with the three-phase domains and A2-B2 two-phase field found to extend to

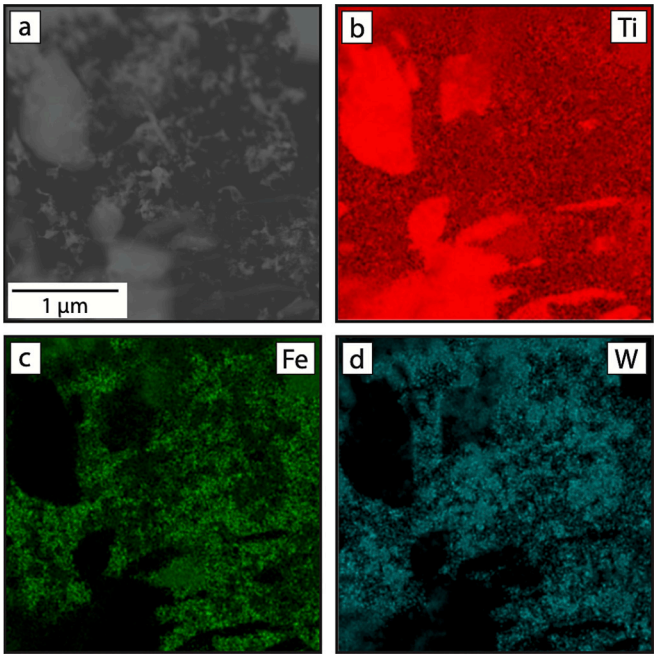

Fig. 6. WT60F solution treated and aged, (a) HAADF-STEM micrograph, followed by EDX elemental maps for (b) Ti, (c) Fe and (d) W.

A2(W,Ti,Fe) at higher W contents. Further, this prediction integrates in a more recent Ti—Fe binary assessment that extends the A2(Ti,Fe,W) to higher Ti content, and includes B2 TiFe(W) off-stochiometric binary and ternary solubility (no longer considered a line/point compound, as in [10]). The ternary prediction at 1250 °C also indicates that while the prior inter-dendritic regions were considered to be A2(Ti,W,Fe) (by SEM-EDX and XRD), at the 1250 °C heat treatment temperatures these are most likely liquid(Ti,W,Fe) that then solidifies to A2 on cooling to room temperature. These composition results show that at high temperature the W bcc solid solution has good solubility for Ti (around 20 at.%) and a lesser amount for Fe (around 5 at.%). The liquid(Ti,W,Fe) single-phase composition is reported as having Fe solubility around 40 at.% at 1250 °C with some dissolved W 5–10 at.%. Furthermore, the B2 TiFe(W) phase can be seen to include off-stochiometric solubility for both W and Ti.

Fig. 5 shows a prediction of the three-phase field present between A2 (W,Ti,Fe), liquid(Ti,Fe,W) and TiFe(W) phases at 1250 °C. This region is therefore surrounded by three two-phase regions, on each of its three sides. By building up a new ternary determination at 1250 °C, a better understanding of the phases that form in W-Ti-Fe can be gained, helping to influence the development of the next W-Ti-Fe alloys, especially when paired with new thermodynamic modelling assessments [9] and bcc-superalloys databases to enable Integrated Computational Materials Engineering (ICME) design [12].

3.5. Transmission Electron Microscopy (TEM)

TEM of an aged WT30F alloy with microstructure similar to Fig. 4 has previously been demonstrated to exhibit a β W(Ti,Fe) with β' TiFe (W) bcc-superalloy microstructure [9]. This work included STEM-EDX identifying co-location of Ti and Fe to the precipitates, as well as diffraction analysis to validate the bcc nature of the W matrix, and B2 ordered-bcc nature of the TiFe(W) precipitates.

Here we have used STEM to study the Ti-rich WT60F alloy in the aged condition after 80 h at 750 °C Fig. 6. The high-angle annular dark-field imaging (HAADF) STEM image revealed similar features to those observable by SEM BS Fig. 4a in the Ti-rich domains (away from the W dendrites and unmelted W). Further study of these features with STEM-

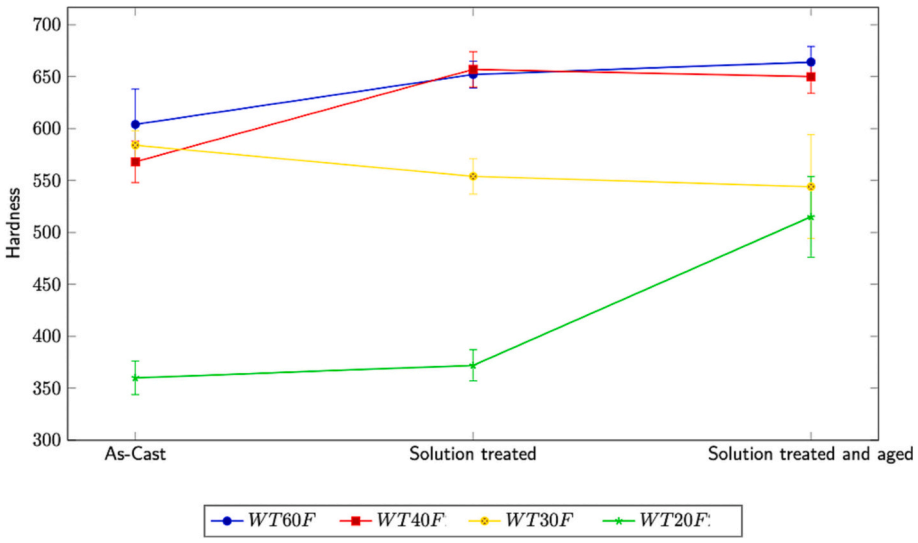

Fig. 7. Microhardness values (HV) of all W-Ti-Fe alloys in all conditions, plotted across each heat treatment stage to show progression of their hardness.

EDX found that the precipitates were nearly pure Ti, indicative of a transformation of A2(Ti,W,Fe) -> A2(Ti,W,Fe) + A3Ti(Fe,W).

3.6. Microhardness

To get basic mechanical properties of these alloys, and to test if they showed an ageing response, Vickers microhardness tests were carried out across the entire set. The results are shown graphically in Fig. 7 (values tabulated in Table 3, appendix). The WT30-60F alloys show high hardness values HV1 of 550 to 650 HV across the series and heat treatment conditions. No pronouced aged hardening was observed, apart from for WT20F. However, these findings are used cautiously due to macrosegregation and porosity within the alloys due to the challenge of arc melting tungsten. It was noted in a number of tests that some heat treated samples exhibited the formation of slip-bands on the corners of the indents, indicating some ductility had occurred in the material. Additionally, no cracks were observed in the indents as occurs in ceramics or materials with a fracture toughness of <10 MPa.m$^{1/2}$ [13,14]. This shows some promising results in regard to reducing the brittle nature of tungsten at room temperature, however, further tests, such as Charpy impact tests, will need to be carried out to begin to confirm this and in particular to evaluate the ductile-to-brittle-transition-temperature. Additionally, more mechanical tests should be carried out on these samples, such as tensile tests, to better understand each alloy's yield strength, ultimate strength and plastic deformation behaviour.

4. Conclusion

Despite challenges in melting tungsten alloys and the resultant macro-segregation, W-Ti-Fe has demonstrated the possibility of casting high W-content alloys to allow for the evaluation of the stable phases that occur in W-rich W-Ti-Fe alloys. Through heat treatments a two-phase microstructure of W-rich A2(W,Ti,Fe) (bcc) prior dendritic and B2 TiFe(W), or A2(Ti,W,Fe) prior inter-dendritic regions, as identified by SEM-EDX. TEM has previously shown that nano-scale precipitates of B2 TiFe(W) form in the W-rich dendrites of similar alloys [9]. Here we used STEM to investigate the A2(Ti,Fe,W) interdendritic regions of the most Ti rich WT60F alloy aged at 750 °C, where formation of A3 alpha Ti phase was indicated, suggestive of an transition A2(Ti,W,Fe) -> A2 + A3. The majority of alloys were shown to possess high hardness values HV1 of 550 to 650 HV, however, a determination of the ductility in these alloys is still needed. The W-Ti-Fe ternary system has been identified to uniquely enable β-β' (A2-B2) 'W-superalloy' microstructures, however, further work is needed to optimise such alloys and establish their range properties.

Author statement

Neal Parkes, led the manuscript preparation, bringing together of data and anaylsis.

Russel Dodds, undertook key experimental work and analysis as well as early writing.

Andy Watson, provided the preliminary thermodynamic assessment and document review.

David Dye, aided the design and co-supervised the study.

Chris Hardie, aided the design and co-supervised the study.

Samuel A Humphry-Baker, supported experiments, design & co-supervision of the study.

Alexander J Knowles, designed the study and supervised the work.

Declaration of Competing Interest

The authors declare that they have no known competing financial interests or personal relationships that could have appeared to influence the work reported in this paper.

Data availability

Data will be made available on request.

Acknowledgements

A.J. Knowles gratefully acknowledges funding from a UKRI Future Leaders Fellowship (MR/T019174/1), Royal Academy of Engineering Research Fellowship (RF\201819\18\158), and EUROfusion Researcher Grant (AWP17-ERG-CCFE/Knowles).

Appendix A. Appendix

Table 3
Microhardness values for the tungsten-titanium-iron alloys, in as-cast, solution treated and solution treated and aged conditions, using 1 kg weight with 10 s dwell. Values averaged over six measurements with S.D.

Alloy Designation	As-cast	Solution treated	Solution treated and aged
Alloy	HV1	HV1	HV1
WT60F	604 ± 34	652 ± 13	664 ± 15
WT40F	568 ± 20	657 ± 17	650 ± 16
WT30F	584 ± 14	554 ± 17	544 ± 50
WT20F	360 ± 16	372 ± 15	515 ± 39

References

[1] R. Doerner, M. Baldwin, T. Lynch, J. Yu, Retention in tungsten resulting from extremely high fluence plasma exposure, Nucl. Mater. Energy 9 (2016) 89–92.
[2] E. Lassner, W. Schubert, Tungsten Properties, Chemistry, Technology of the Elements, Alloys, and Chemical Compounds, Springer Science & Business Media, 1999.
[3] R. Herschitz, D. Seidman, An atomic resolution study of homogeneous radiation-induced precipitation in a neutron irradiated W- 10at.% Re alloy, Acta Metall. 32 (1984) 1141–1154.
[4] Z. Dong, Z. Ma, L. Yu, Achieving high strength and ductility in ODS-W alloy by employing oxide@w core-shell nanopowder as precursor, Nat. Commun. 12 (2021) 5052.
[5] H.J. Ryu, H. Hong Soon, Fabrication and properties of mechanically alloyed oxide-dispersed tungsten heavy alloys, Mater. Sci. Eng. A363 (2003) 179–184.
[6] H. Bei, E. George, Microstructures and mechanical properties of a directionally solidified NiAl-mo eutectic alloy, Acta Mater. (2005) 69–77.
[7] C. Stallybrass, A. Schneider, G. Sauthoff, The strengthening effect of (Ni,Fe)Al precipitates on the mechanical properties at high temperatures of ferritic Fe-Al-Ni-Cr alloys, Intermetallics (2005) 1263–1268.
[8] A. Knowles, T. Jun, A. Bhowmik, N. Jones, T. Britton, F. Giuliani, D. Dye, A new beta titanium alloy system reinforced with superlattice intermetallic precipitates, Scr. Mater. 139 (2017) 71–75.
[9] A. Knowles, D. Dye, R. Dodds, A. Watson, C. Hardie, S. Humphry-Baker, Tungsten-based bcc-superalloys, Appl. Mater. Today 23 (2021), 101014.
[10] C. Qiu, Z. Jin, An experimental study and themodynamic evaluation of the Fe-Ti-W system at 1000C, Scr. Metall. Mater. 28 (1) (1993) 85–90.
[11] A. Knowles, N. Jones, C. Jones, H. Stone, Phase equilibria and properties of ti-fe-mo alloys with ultra-fine lamellar microstructures, in: Proceedings of the 13th World Conference on Titanium, 2016, pp. 1229–1236.
[12] O. Senkov, D. Miracle, K. Chaput, J. Couzinie, Development and exploration of refractory high entropy alloys—a review, J. Mater. Res. (2018) 3092–3128.
[13] A. Knowles, A. Bhowmik, S. Purkayastha, N. Jones, F. Giuliani, W. Clegg, H. Stone, Laves phase intermetallic matrix compos ite in situ toughened by ductile precipitates, Scr. Mater. 140 (2017) 59–62.
[14] A. Bhowmik, H. Stone, Microstructure and mechanical properties of two-phase Cr-Cr2Ta alloys, Metall. Mater. Trans. A 43 (9) (2012) 3283–3292.